JOURNAL OF GEOPHYSICAL RESEARCH, VOL. 103, NO. B12, PAGES 29,895–29,913, DECEMBER 10, 1998

Time functions of deep earthquakes from broadband and short-period stacks

Heidi Houston

Department of Earth and Space Sciences, University of California, Los Angeles

Harley M. Benz

US Geological Survey, Denver, Colorado

John E. Vidale

Department of Earth and Space Sciences, University of California, Los Angeles

Abstract. To constrain dynamic source properties of deep earthquakes, we have systematically constructed broadband time functions of deep earthquakes by stacking and scaling teleseismic P waves from U.S. National Seismic Network, TERRAscope, and Berkeley Digital Seismic Network broadband stations. We examined 42 earthquakes with depths from 100 to 660 km that occurred between July 1, 1992 and July 31, 1995. To directly compare time functions, or to group them by size, depth, or region, it is essential to scale them to remove the effect of moment, which varies by more than 3 orders of magnitude for these events. For each event we also computed short-period stacks of *P* waves recorded by west coast regional arrays. The comparison of broadband with short-period stacks yields a considerable advantage, enabling more reliable measurement of event duration. A more accurate estimate of the duration better constrains the scaling procedure to remove the effect of moment, producing scaled time functions with both correct timing and amplitude. We find only subtle differences in the broadband time-function shape with moment, indicating successful scaling and minimal effects of attenuation at the periods considered here. The average shape of the envelopes of the short-period stacks is very similar to the average broadband time function. The main variations seen with depth are (1) a mild decrease in duration with increasing depth, (2) greater asymmetry in the time functions of intermediate events compared to deep ones, and (3) unexpected complexity and late moment release for events between 350 and 550 km, with seven of the eight events in that depth interval displaying markedly more complicated time functions with more moment release late in the rupture than most events above or below. The first two results are broadly consistent with our previous studies, while the third is reported here for the first time. The greater complexity between 350 and 550 km suggests greater heterogeneity in the failure process in that depth range.

1. Introduction

The physical mechanism permitting deep seismic failure is a long-standing problem of intrinsic interest in geophysics and may have implications as well for the fate of subducting slabs and for shallow seismic failure. Deep earthquakes have been an enigma since their detection over 70 years ago [*Wadati*, 1928]. Current understanding of the rheological behavior of olivine, the major constituent of subducting lithosphere, indicates that at depths greater than a few tens of kilometers the pressure is large enough that frictional forces should not permit brittle/frictional failure. Even with a low coefficient of friction, normal stresses are too great to permit brittle frictional processes [*Scholz*, 1990]. Deviatoric stresses would have to be enormous to overcome the friction, and extrapolations of olivine flow laws imply that rocks should flow rather than break to relieve the stress.

A number of mechanisms have been proposed to explain the observed deep seismicity, including plastic instabilities [*Hobbs and Ord*, 1988], shear-induced melting [*Griggs and Baker*, 1969], instabilities accompanying recrystallization [*Ogawa*, 1987], and polymorphic phase transformations [*Sung and Burns*, 1976; *Kirby*, 1987; *Meade and Jeanloz*, 1989]. Recently, a particular version of the latter mechanism, transformation faulting in metastable olivine, has received increased attention

Paper number 98JB02135.
0148-0227/98/98JB-02135$09.00

because laboratory experiments on silicate and germanate olivine revealed a shear instability associated with the transformation of metastable olivine in a deviatoric stress field [e.g., *Green and Burnley*, 1989; *Green et al.*, 1990]. Various properties of transformational faulting have been found to be consistent with many of the seismic signatures of deep earthquakes [*Kirby et al.*, 1991; *Green and Houston*, 1995; *Kirby et al.*, 1996]. However, the recent June 9, 1994, Bolivian earthquake (M_W = 8.2, 636 km depth) appeared to rupture over a larger area than expected and led to suggestions that deep seismic failure must occur by other mechanisms, such as reactivation of preexisting faults [*Silver et al.*, 1995; see also the special issue on the Bolivian earthquake, *Geophysical Research Letters, 22* (16), 1995]. Furthermore, aftershocks of the March 9, 1994, Tonga earthquake (M_W = 7.6, 568 km depth) appear to lie outside the portion of the slab that was previously seismically active [*Wiens et al.*, 1994]. *Houston* [1994], *Stein* [1995] and *Kirby et al.* [1996] suggested that these observations need not preclude transformational faulting, but nonetheless, they do cast doubt on the simplest models of this mechanism. Definitive identification of the process that permits deep seismic failure has remained elusive.

Despite the lack of consensus, recent interest and advances have been considerable and for more details we refer the interested reader to the following reviews. A survey of many of the properties of deep earthquakes is given by *Frohlich* [1989]. The possible role of metastable olivine in deep seismic failure is discussed at length by *Green and Houston* [1995]. The phenomenology of deep seismicity and its possible relation to transformational faulting in metastable olivine is discussed by *Kirby et al.* [1996].

Many studies have been made on the source processes of deep earthquakes. Most of the techniques developed and applied to determine source processes or properties of shallow earthquakes also have been applied to deep events. In particular, the durations of deep earthquakes have been studied by a number of workers [e.g., *Mikumo*, 1971; *Chung and Kanamori*, 1980]. However, these studies of duration used long-period waveforms, which lack precise definition of event termination. Recent work by *Vidale and Houston* [1993] utilized stacks of many short-period waveforms from regional arrays to measure durations of deep earthquakes. More recently, *Bos et al.* [1998] stacked global sets of broadband waveforms and fit triangles to the stacks to estimate durations of deep events. Stress drops have been obtained in a number of studies with a variety of approaches and assumptions. In general, the studies find a large scatter in stress drops with possible small differences with depth (see discussion by *Frohlich* [1989]). Source time functions of individual deep earthquakes have been obtained by numerous studies (e.g., the special issue on the Bolivian earthquake in *Geophysical Research Letters*, 1995). However, owing to the difficulty of the data analysis, systematic studies of deep earthquake time functions are far fewer. *Kikuchi and Fukao* [1987] analyzed long-period World-Wide Standardized Seismograph Network *P* waves of 18 intermediate and deep earthquakes, and a follow-up study analyzed similar data for 28 more events [*Sugi et al.*, 1989]. Unfortunately, the large variation in event moment due to the power-law distribution of earthquake sizes hampers the direct comparison of time functions. In sum, observed differences in the source properties of shallow, intermediate, and deep earthquakes are subtle, save for the lower aftershock productivity for events deeper than about 100 km [*Frohlich*, 1987].

The goal of this paper is to systematically examine time functions of deep earthquakes for their shape, duration,

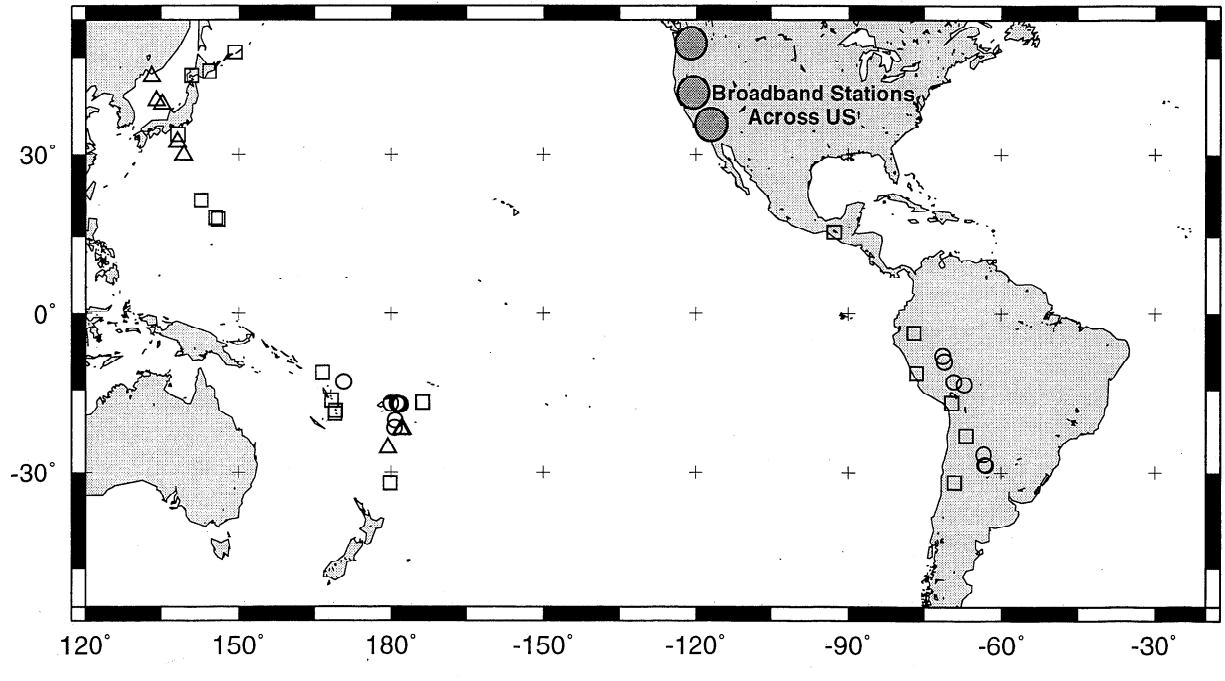

Figure 1. Map of earthquake sources. Squares, triangles, and circles denote events in the depth ranges 100-350 km, 350-550 km, and 550-650 km, respectively. Large shaded dots denote the short-period regional arrays used here.

Table 1. Estimated Rupture Durations of the Events Analyzed in This Study

Event Date	Time, UT	Latitude	Longitude	Depth, km Hvd	Depth, km ISC	Moment, Nm	Duration, s	Scaled Duration, s
July 11, 1992	1044:20.9	-22.28	-178.51	394	381	7.76e19	19.6	9.9
Aug. 8, 1992	0659:40.5	41.94	140.72	124	127	1.80e18	3.8	6.7
Aug. 29, 1992	1919:07.5	33.16	138.02	309	309	2.88e18	3.3	5.0
Aug. 30, 1992	2009:06.9	-17.74	-178.77	574	573	4.65e18	5.7	7.4
Oct. 30, 1992	0249:49.4	29.97	138.93	408	406	4.88e18	8.0	10.2
Nov. 12, 1992	2228:58.4	-22.35	-178.08	378	368	2.29e18	5.6	9.2
Jan. 15, 1993	1106:05.0	43.40	143.26	100	100	2.72e20	24.0	8.0
Jan. 18, 1993	0118:08.1	18.38	145.71	158	169	2.15e18	5.3	8.8
Jan. 19, 1993	1439:26.7	38.63	133.46	462	455	6.31e18	6.3	7.3
March 21, 1993	0504:59.0	-17.97	-178.53	608	584	3.29e18	3.7	5.4
April 16, 1993	1408:38.8	-17.69	-178.88	592	568	2.62e19	9.3	6.7
April 18, 1993	0916:21.7	-11.61	-76.55	113	90	2.81e18	7.0	10.7
April 24, 1993	0954:21.2	-17.73	179.81	610	600	2.72e18	5.4	8.3
May 6, 1993	1303:19.3	-8.47	-71.49	595	586	1.80e18	3.7	6.6
May 24, 1993	2351:22.7	-23.22	-66.64	232	238	3.34e19	13.8	9.2
June 8, 1993	2317:41.4	-31.59	-69.22	124	113	3.16e18	5.5	8.1
Oct. 11, 1993	1554:22.4	32.00	137.85	364	365	2.45e19	10.0	7.4
Jan. 10, 1994	1553:49.6	-13.31	-69.39	604	589	2.50e19	9.0	6.6
Feb. 11, 1994	2117:31.5	-18.81	169.16	223	204	2.13e19	7.0	5.4
Feb. 24, 1994	1525:35.8	-17.37	-174.36	128	124	1.80e18	4.0	7.1
March 9, 1994	2328:07.7	-17.77	-178.50	568	564	3.07e20	13.5	4.3
March 14, 1994	2051:25.4	15.98	-92.40	168	169	2.25e19	9.0	6.9
March 31, 1994	2240:53.4	-21.95	-179.58	607	591	6.56e18	3.3	3.8
April 29, 1994	0711:30.3	-28.30	-63.17	566	573	2.54e19	9.5	7.0
May 4, 1994	0637:37.9	-17.07	168.27	225	221	1.85e18	3.8	6.7
May 10, 1994	0636:28.7	-28.50	-63.06	603	605	2.77e19	7.0	5.0
June 9, 1994	0033:16.4	-13.83	-67.56	647	637	2.63e21	42.0	6.6
July 21, 1994	1836:31.7	42.30	132.89	489	473	1.10e20	15.2	6.8
Aug. 19, 1994	1002:51.8	-26.65	-63.38	563	565	5.57e18	4.0	4.9
Aug. 22, 1994	1726:38.2	-11.50	166.42	150	148	1.99e18	4.4	7.5
Oct. 16, 1994	0510:03.3	45.74	149.22	121	139	1.37e19	13.0	11.7
Oct. 27, 1994	2220:31.0	-25.79	179.35	541	549	1.13e19	10.0	9.6
Nov. 4, 1994	0113:20.8	-9.33	-71.31	619	598	1.50e18	3.8	7.2
Dec. 12, 1994	0741:55.4	-17.50	-69.65	161	151	2.58e18	4.0	6.3
Dec. 27, 1994	1732:52.5	-32.00	179.87	226	228	3.96e18	9.0	12.3
Dec. 30, 1994	1512:26.9	18.59	145.27	228	235	3.14e18	8.0	11.8
Jan. 17, 1995	1654:12.0	-20.87	-179.23	649	637	3.53e18	4.0	5.7
March 31, 1995	1401:40.8	38.15	135.06	366	365	2.09e18	4.1	6.9
April 8, 1995	1745:18.1	21.80	142.63	281	319	2.50e18	3.4	5.4
April 13, 1995	0234:38.3	-13.40	170.40	646	640	2.06e18	4.5	7.6
May 2, 1995	0606:05.9	-3.85	-76.96	113	103	1.27e19	10.0	9.2
June 29, 1995	1224:03.9	-19.46	169.24	143	144	9.33e18	5.0	5.1

Hvd, Harvard; ISC, International Seismological Centre. Read 7.76e19 as 7.76×10^{19}.

complexity, and rate of initiation. We seek to illuminate the processes that start and stop rupture and provide the complexity that radiates high frequencies. Our approach is to stack teleseismic broadband records of deep earthquakes to determine time functions, after aligning the first breaks. We take advantage of broadband data, only recently available, which provide a more direct window into the source. Our treatment of the data (novel to our knowledge) is made possible by the increasing density of broadband stations. Also novel is our comparison of short-period and broadband data, which leads to more accurate estimates of duration. This approach provides moment-rate functions rapidly and overcomes some problems other approaches have with resolving the later part of rupture. Finally, we scale the moment-rate functions, removing the effect of moment, which ranges over 3 orders of magnitude, to facilitate comparison of events. Observed variations with depth or moment may provide insight into deep failure processes and the physical mechanism of deep-focus earthquakes.

2. Determining Broadband Time Functions by Stacking Teleseismic *P* Waveforms

2.1 Constructing Broadband Stacks

We analyzed 42 events between 100 and 660 km depth that occurred between July 1, 1992, and July 31, 1995, with seismic moments greater than 1.8×10^{18} N m (Figure 1 and Table 1). The data consist of teleseismic *P* waveforms (distances from 30° to 90°), recorded in North America by the U.S. National Seismic Network, TERRAscope, and the Berkeley Digital Seismic Network. For each event we constructed a stack (sum) of the available broadband displacement records. Stacking seismograms reduces noise produced by incoherent reverberations at the stations. Random noise is reduced by the square root of the number of records stacked [*Kanasewich*, 1981]. The procedure was to remove the broadband instrument response, discard noisy stations, carefully line up the *P* waves on the first break or on a prominent sharp feature early in the waveform, normalize,

and sum the records. To remove the instrument response, we removed the trend, tapered, and deconvolved the instrument using the Seismic Analysis Code (SAC) over the frequency range 0.01 to 8 Hz. Typically, 8 to 15 broadband stations were stacked for each event.

2.2 Constructing Short-Period Stacks

We also constructed short-period stacks using the much more numerous short-period stations of the Northern California Seismic Network, Southern California Seismic Network, and Washington Seismic Network. Because many more short-period records exist and can be included in a stack, we can achieve better noise suppression with short-period stacks. In particular, the initiation and termination of rupture are often better defined than in an individual broadband record, or even in the broadband stack. The procedure, similar to that of *Vidale and Houston* [1993], was to discard noisy or problem stations, then to line up the *P* waveforms on a common sharp feature early in the waveform and to sum the records. The instrument response was not removed. Typically, 50 to 150 stations were summed for each event. For a particular event, we used data from the regional array that was most readily available. Previous experience has indicated that the short-period stacks from the above three regional arrays closely resemble each other [*Vidale and Houston*, 1993].

2.3 Aligning Broadband and Short-Period Stacks

We carefully registered the broadband to the short-period stack for each earthquake, examined the two together, and picked the initiation and termination of moment release, using both types of data but relying primarily on the short-period stack. Our previous work using short-period stacks of *P* waveforms of deep earthquakes indicated that owing to effective noise suppression, short-period stacks often reveal the ending of rupture exceptionally clearly [*Houston and Vidale*, 1994; *Vidale and Houston*, 1993]. Figure 2 illustrates the procedure used to register the broadband stack to the short-period stack.

Figure 3 shows the registered broadband and short-period stacks for all events in this study. Depth phases are prominent on some of the seismograms from events shallower than 170 km. All stacks were carefully aligned to begin at time 0; our pick for the termination of rupture is shown by a short vertical line. Amplitudes have been normalized to 1. Many similarities are evident between the broadband and short-period stacks, including the overall shape, as well as short-period features. The envelope of a time series is given by the square root of the sum of the squares of the time series and its Hilbert transform [*Kanasewich*, 1981]. Many of the envelopes of the short-period stacks are similar in shape to the broadband displacement stacks even though the short-period instrument was not removed (Figure 4).

2.4 Duration of Rupture

Rupture durations are estimated from inspection of the short-period and broadband data together and are listed in Table 1. In order to scale the stacks to remove the effect of moment, it is necessary to know the total moment, of course, and either the true stack amplitude (in moment rate) or the duration of rupture. Moments are taken from the Harvard Centroid Moment Tensor (CMT) catalog [*Dziewonski and Woodhouse*, 1983]. Amplitudes are usually strongly contaminated by different site responses at each station. Duration is also notably difficult to determine because many events appear to die away gradually and their termination is hidden in the coda. However, the use of high-resolution short-period stacks aids greatly in the determination of duration. Our stacking procedures result in exceptionally noise-free broadband stacks that provide the shape of the source time function. The shape, together with the measured duration and CMT moment, can be used to determine true amplitudes for the source time functions as discussed in section 3.

For earthquakes deeper than 100 km the depth-reflected phases are separable from the direct body wave so that the body-wave displacement record is the source time function convolved with the effect of attenuation, which is discussed in section 4. Figure 5 compares the broadband displacement stacks constructed here with source time functions for the March 9, 1994, Tonga (M_W=7.6) and June 9, 1994, Bolivia (M_W=8.2) deep earthquakes obtained with more conventional methods. For the Tongan event, *P* waveforms all across the United States are similar but change polarity during the event due to a change in focal mechanism [*McGuire et al.*, 1997]. Because of the significance of this large, well-studied event we made a special effort to salvage the time function. An "adjusted" broadband stack was constructed from the broadband stack by taking the absolute value. In Figure 5 the heavy line, labeled moment release rate, was determined by *McGuire et al.* [1997] by time-domain inversion of a large set of teleseismic and regional waveforms. For the Bolivian event the moment release rate was taken from *Ihmle and Jordan* [1995], who performed a spectral-domain inversion of body waves, traveling modes, and free oscillations. Although details of the timing of subevent arrivals differ, in overall shape, general character, duration, and even the rate of initiation the broadband stacks are quite similar to time functions determined by more traditional methods (Figure 5). The possible effects of rupture directivity on the broadband stacks are discussed in section 4. In the rest of this paper, we will use and refer to the broadband stacks as time functions.

3. Scaling Time Functions to a Common Size

The seismic moments of our set of events vary by a factor of 2000 (Figure 6), so they cannot be plotted effectively on the same scale. It is therefore advantageous to scale the time functions to a common size for the purposes of comparison. For our procedure (and most methods of scaling time functions) the event duration must be known or assumed. However, a reliable estimate of event duration is usually hard to come by because moment release often ends gradually and can be difficult to detect on a broadband record. An advantage of this study comes from our use of high-resolution short-period stacks of many stations, which more clearly reveal the event starting and stopping times.

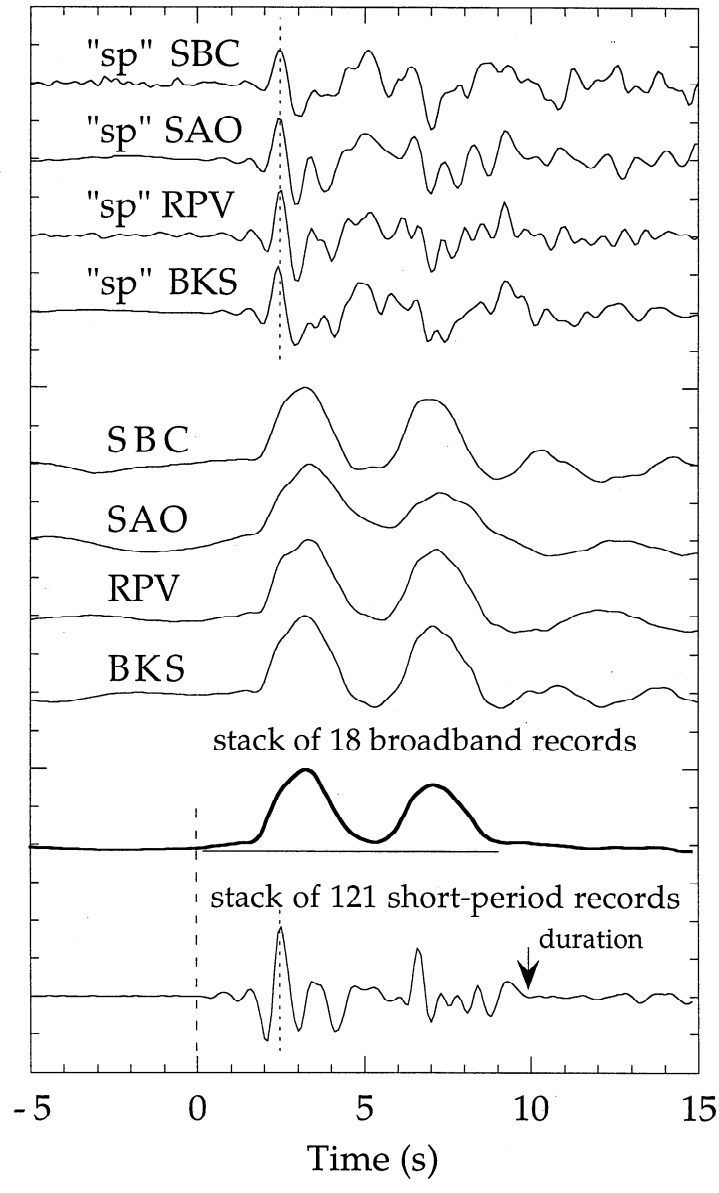

Figure 2. Method of alignment for stacking broadband *P* waveforms, using the October 27, 1994 event as an example. The broadband displacement records are convolved with a short-period instrument response to emphasize high-frequency features. The short-period stack of 121 stations from a regional array is used as a guide to establish a suitable sharp, prominent feature of the simulated short-period records. The arrival time of this feature is picked on each of the simulated records (dotted line); then the broadband records are stacked using the alignments determined from the simulated records. The origin time of the broadband stack (dashed line) can be determined from the timing of the prominent feature on the short-period stack, for which the initiation of rupture is clearly resolvable, or it can be picked directly from the broadband stack. The overall duration of the event is readily picked from the short-period stack (arrow). Note that the preevent noise and the coda in the individual broadband records have been greatly reduced by the stacking procedure.

We utilize a two-step procedure to scale time functions to a common size (Figure 7). First, to obtain a moment-rate time function, the amplitude of the broadband displacement stack is set so that over the measured duration the area under the stack is equal to the event's Harvard CMT moment. Accurate durations are necessary to recover the correct moment-rate amplitudes. Second, the time axis and the amplitude are simultaneously adjusted (squeezed or stretched) according to natural scaling relations, so that the area under the resulting scaled time function is reduced or increased to the same reference value $M_{0\text{ref}}$ for all events. That is, the time axis is divided by $(M_0^i)^{1/3}$, following Figure 6a and numerous studies that have found that event duration is proportional to the cube root of moment [e.g., *Kanamori and Anderson*, 1975; *Furumoto and Nakanishi*, 1983; *Vidale and Houston*, 1993]. Certainly, this proportionality is expected from the definition of moment and the empirical observation of

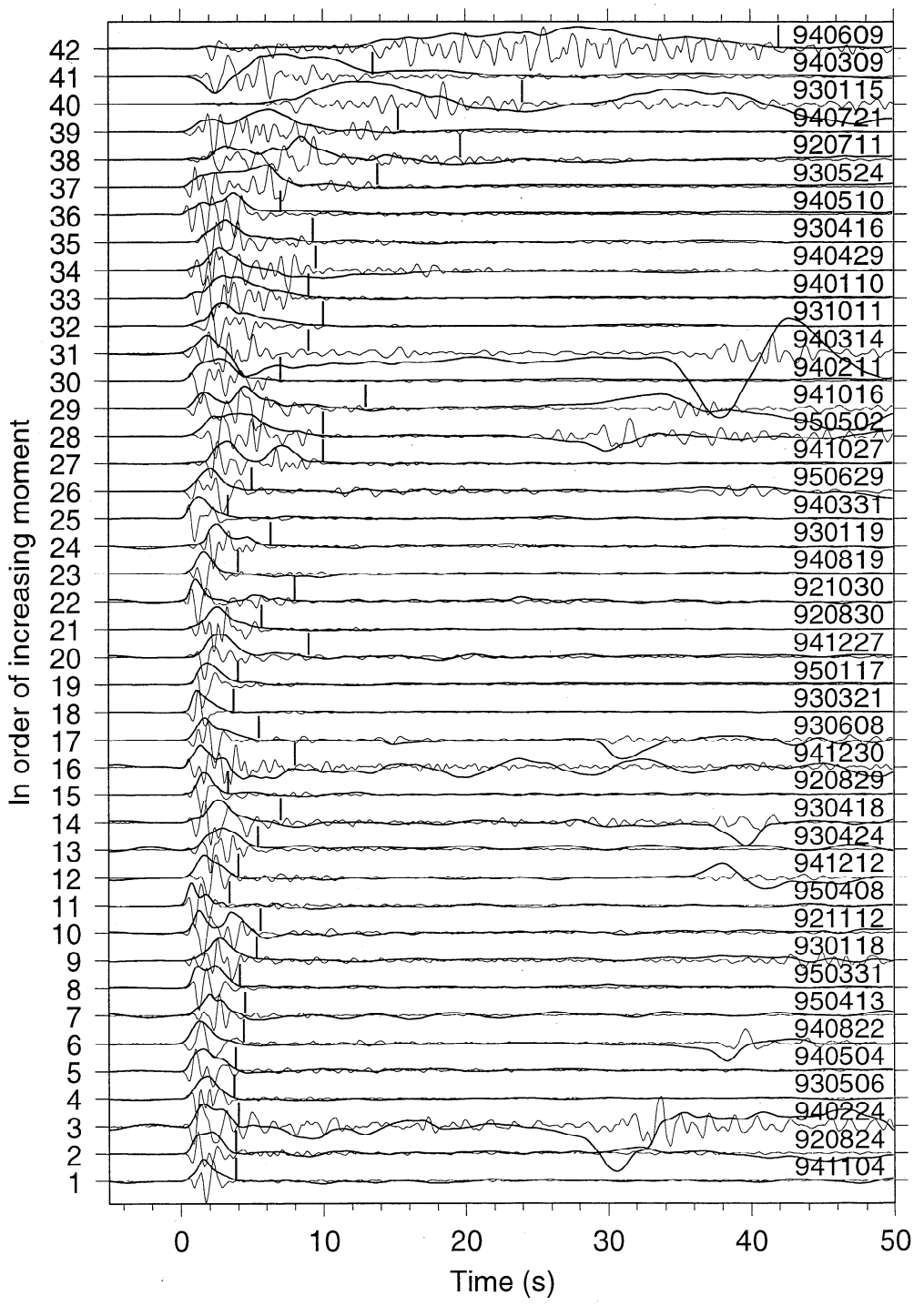

Figure 3. Broadband displacement stacks of *P* waveforms (thick lines) and stacks of short-period P waveforms from regional arrays (thin lines) for each event in this study. Events are ordered by increasing seismic moment. Date of each event is given on the right-hand side. Short vertical lines indicate the event durations picked from these data. The instrument response has not been removed from the short-period stacks. Nonetheless, many similarities between the broadband and short-period stacks are evident. Events 3 and 16 are significantly contaminated by noise and are discarded; event 31 is discarded because it is almost completely nodal and thus cannot be used for the purposes of this study. Prominent depth phases are seen on the figure for many of the events with depths less than 170 km.

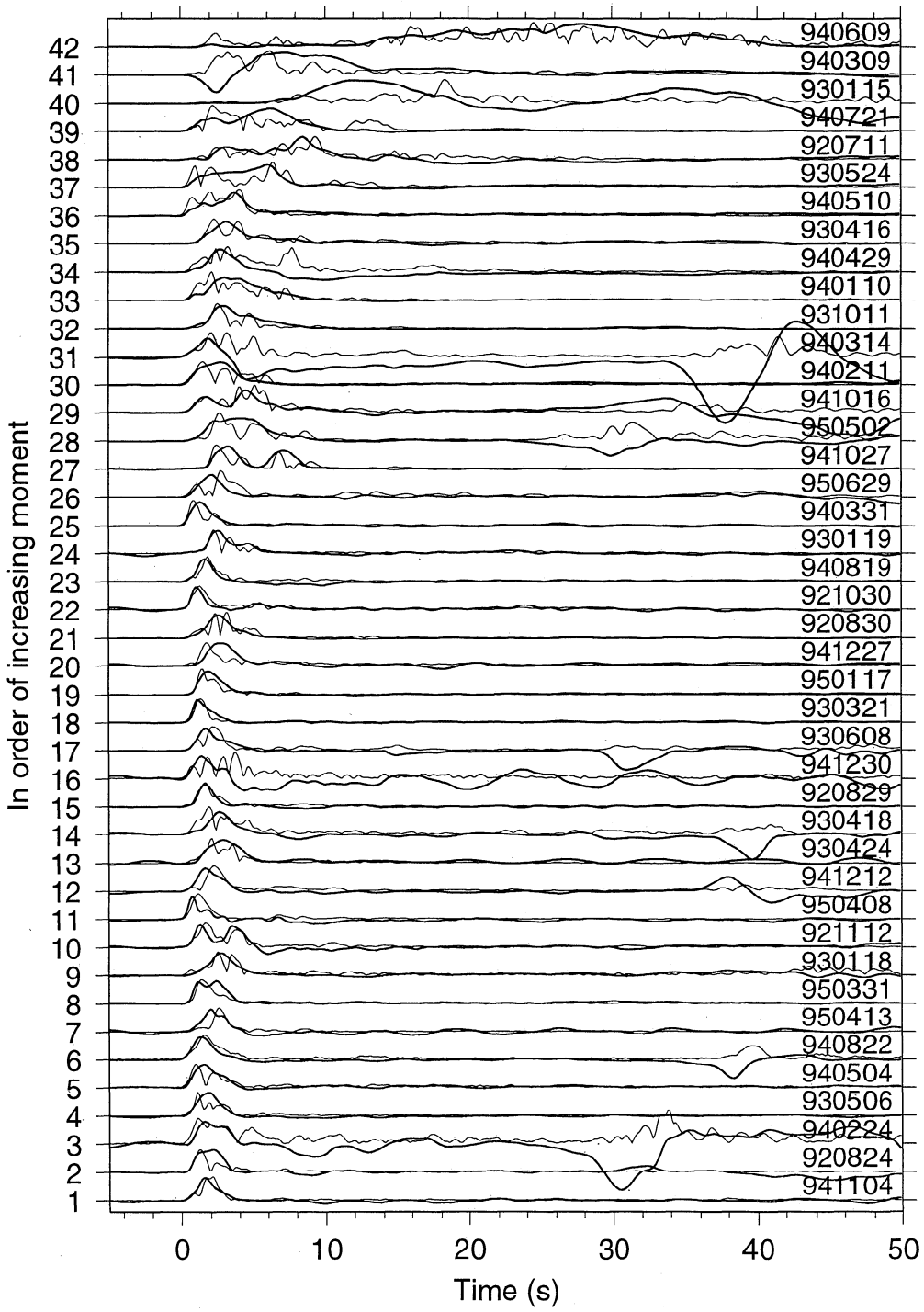

Figure 4. Envelopes of the short-period stacks (thin lines) compared to broadband displacement stacks (thick lines) for each event in this study. Events are shown in order of increasing seismic moment. Although the instrument response has not been removed, many envelopes are similar in shape to the broadband displacements.

earthquake self-similarlity over many orders of magnitude [*Abercrombie*, 1995]. To preserve units, self-similarity, and the relation between moment and area under the time function, amplitudes must be divided by $(M_0^i)^{2/3}$. Here again, the assumed duration affects the area under the time function. Since that area represents moment, the second step normalizes all events to the reference moment.

In mathematical terms, for event i with moment M_0^i, the scaled time function $u^i_{\text{scaled}}(t)$ is given by

$$u^i_{\text{scaled}}(t) = \left(\frac{M_{0\text{ref}}}{M_0^i}\right)^{\frac{2}{3}} u^i(\tau), \quad t = \left(\frac{M_{0\text{ref}}}{M_0^i}\right)^{\frac{1}{3}} \tau, \qquad (1)$$

where t is scaled time, τ is unscaled time, $u^i(\tau)$ is the

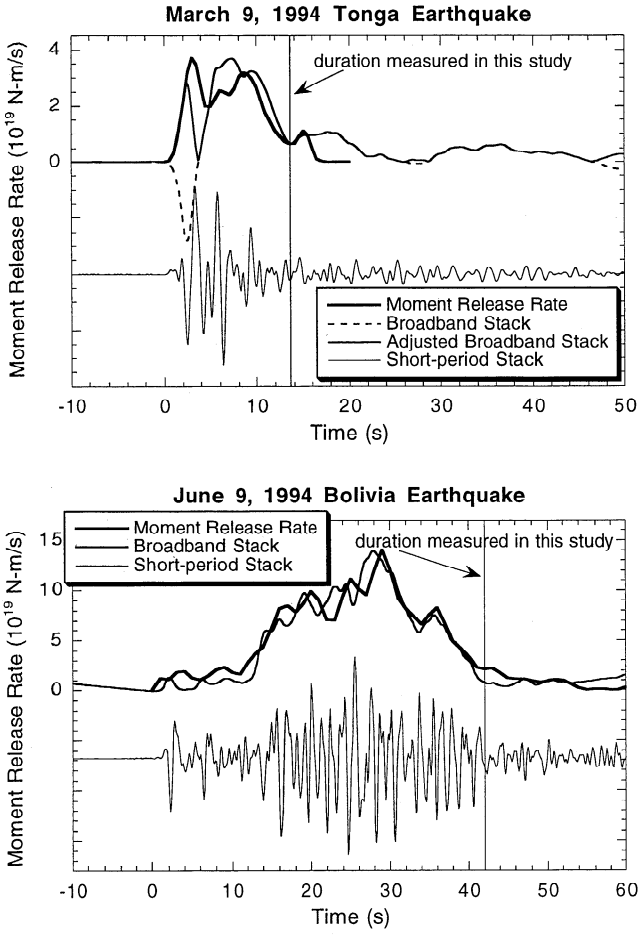

Figure 5. Comparison of broadband and short-period stacks with time functions determined by other studies. (top) March 9, 1994, Tonga earthquake. Since the *P* wave in North America changes sign due to a change in focal mechanism, we constructed an adjusted broadband stack from the broadband stack by taking the absolute value. The moment release rate (heavy line) was determined by *McGuire et al.* [1997]. (bottom) June 9, 1994, Bolivia earthquake. The moment release rate (heavy line) was taken from *Ihmle and Jordan* [1995].

unscaled moment-rate function, and $M_{0\text{ref}}$ is the reference moment taken to be 10^{19} N m, which corresponds to M_W = 6.6. Thus the area under each scaled time function is exactly 10^{19} N m. The scaled time function is set to 0 at times before the initiation time and after the termination time. To ensure that $u^i(\tau_0^i) = u^i{}_{\text{scaled}}(t_0^i) = 0$, where τ_0^i and t_0^i are the unscaled and scaled duration of event i, any linear trend in $u^i(\tau)$ between $\tau = 0$ and $\tau = \tau_0^i$ is removed. That is, to remove a step at the end of the scaled time function, the end point is "pulled down" (or up) to 0 and the other points adjusted linearly.

We term the above procedure moment scaling (Figure 8). We have also developed an analogous procedure termed duration scaling, in which the time functions are scaled to have the same duration. In this case, the time axis is scaled so that the termination of the time function occurs at a reference value $t_{0\text{ref}}$. We chose 6 s for $t_{0\text{ref}}$, an appropriate value for deep events with the reference moment 10^{19} N m [e.g., *Vidale and Houston*, 1993]; however, the exact value of the reference duration is not important for the purpose of comparison of scaled time functions. Finally, the amplitudes are scaled so that the area under each time function equals the reference moment.

Mathematically, for event i with moment-scaled duration t_0^i, the duration-scaled time function $u^i_{\text{d-scaled}}(s)$ is given by

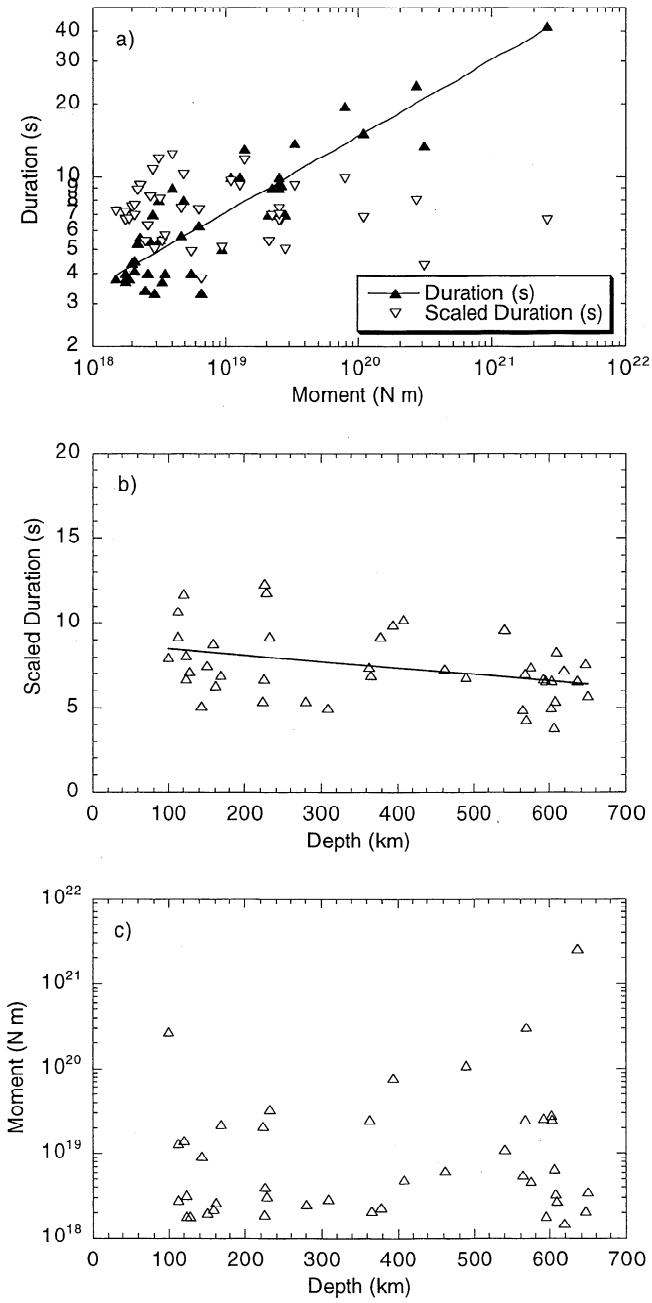

Figure 6. (a) Duration and scaled duration versus seismic moment. Scaled duration is duration divided by the cube root of the seismic moment relative to a reference moment of 10^{19} N m. The line is a least squares fit to the durations and has a slope of 0.32 (correlation coefficient 0.94). Note the lack of dependence of scaled duration on moment, which indicates appropriate scaling. (b) Scaled duration versus depth. The line is a least squares fit to the data. (c) Moment versus depth.

$$u^i_{\text{d-scaled}}(s) = \left(\frac{t^i_0}{t_{0\text{ref}}}\right) u^i_{\text{scaled}}\left(\frac{t^i_0}{t_{0\text{ref}}} s\right), \quad (2)$$

where s is duration-scaled time. Moment and duration scaling are compared in section 4.

4. Effects of Attenuation, Directivity, and Geometrical Spreading

Attenuation refers to the decrease in amplitude of seismic waves due to anelastic and scattering processes. High frequencies are most strongly affected. For a study

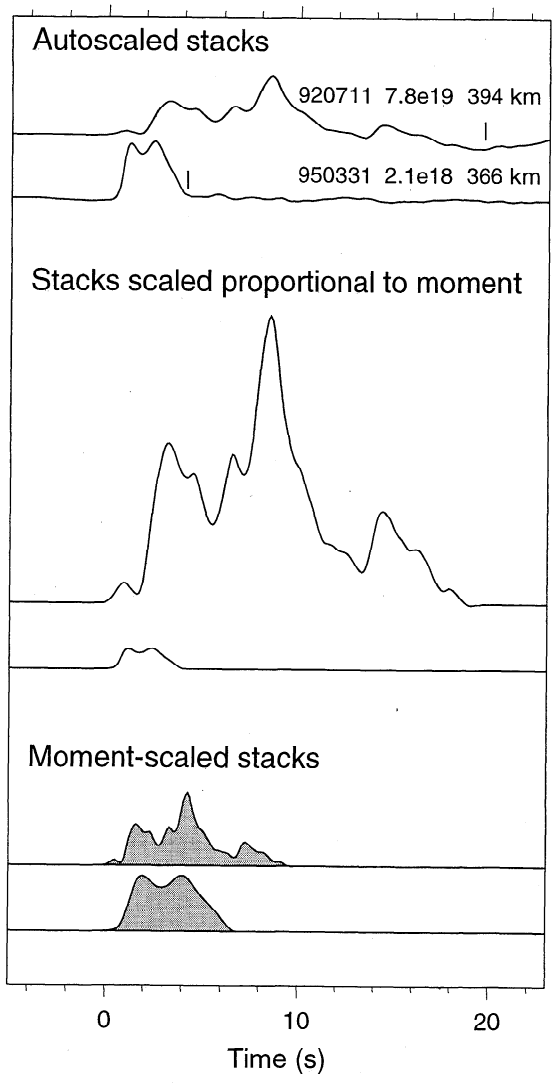

Figure 7. Illustration of the scaling procedure. (top) Autoscaled broadband stacks of P waves from two events, one with CMT moment 40 times greater than the other. Durations were estimated by comparing short-period and broadband data and are marked by vertical lines. (middle) Windowed stacks with amplitudes scaled so that the areas under the waveforms are proportional to moment. These are time functions (moment-rate functions). (bottom) Moment-scaled stacks. Amplitude and timescale of the time functions have been scaled according to equation (1) to remove the effect of moment. The areas under the moment-scaled time functions are equal.

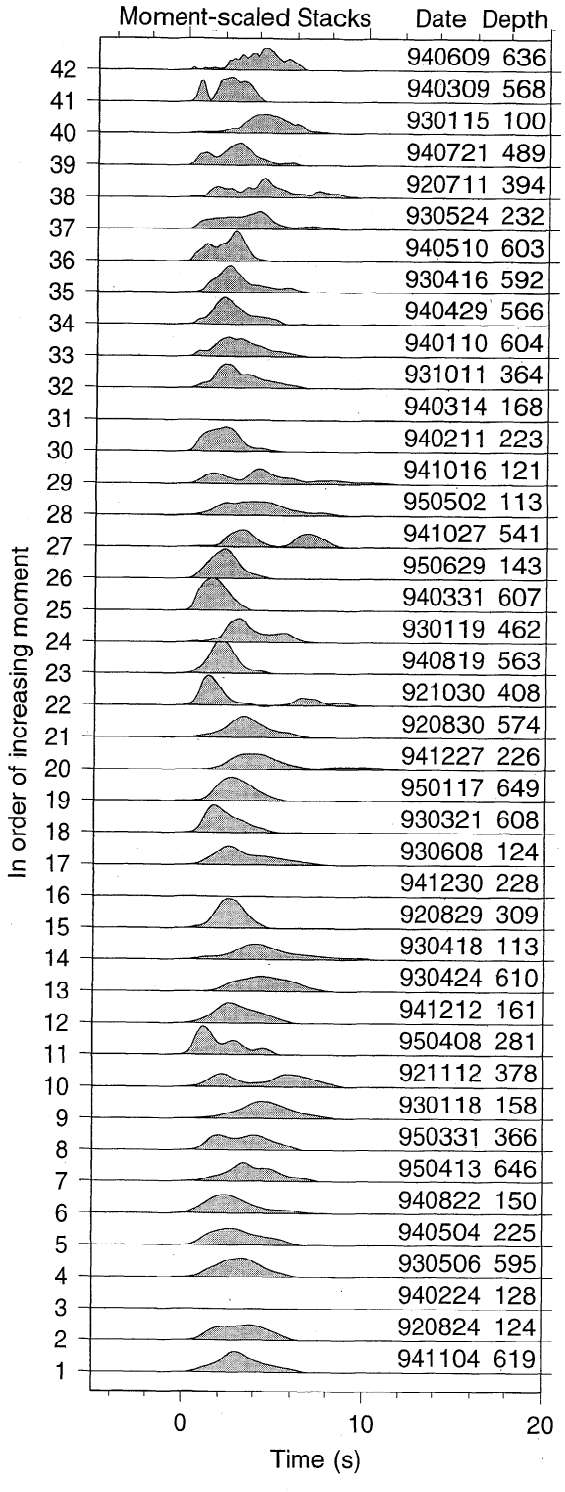

Figure 8. Moment-scaled broadband stacks for all the events in this study. Events are shown in order of increasing event moment before scaling; event moments span more than 3 orders of magnitude. The general similarity in the durations and shapes of the scaled stacks attests to the validity of the scaling. The variation in short-period detail from small to large events is an indication of the effects of attenuation. The area under each time function is the reference moment 10^{19} N m. Each unit increment on the y axis represents a moment release rate of 5.7 x 10^{18} N m/s. Events 3, 16, and 31 were omitted because they were judged too noisy or too nodal (see Figure 3).

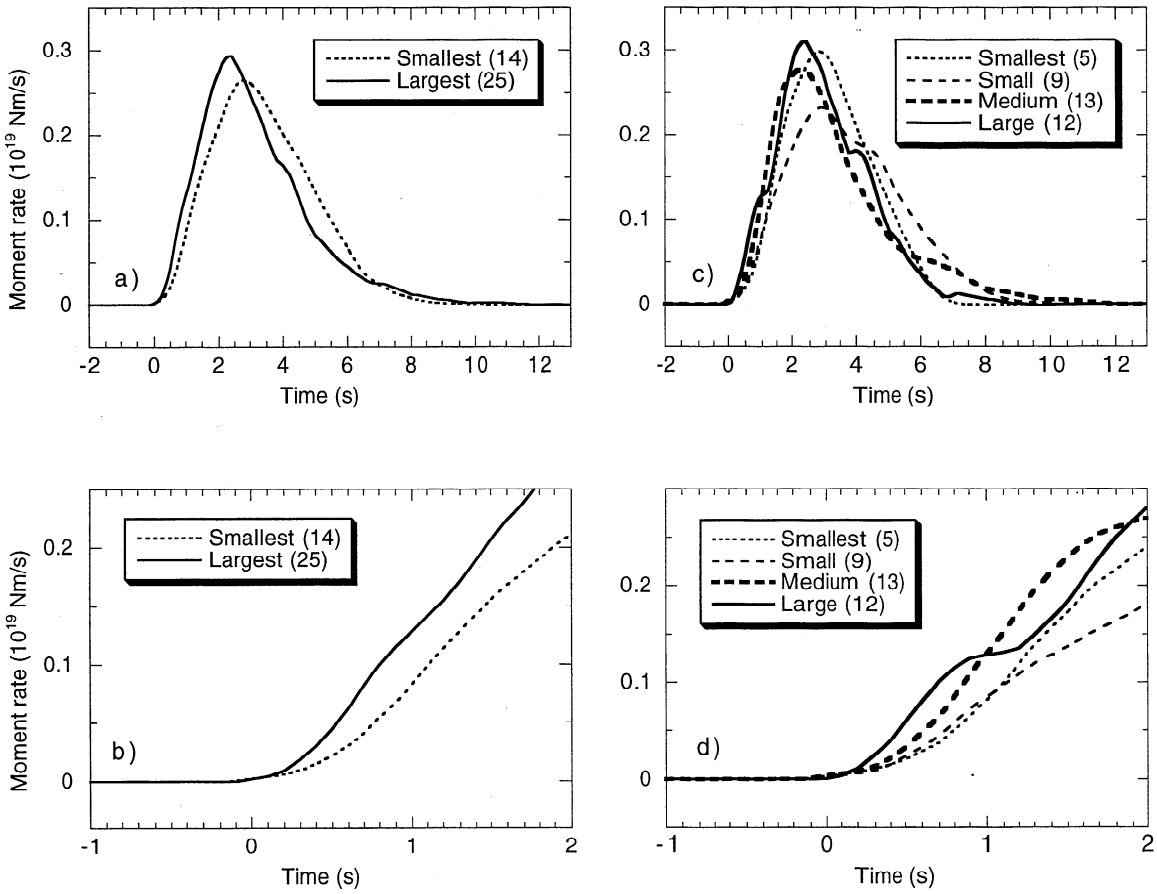

Figure 9. Averages of moment-scaled stacks grouped by event size. (a) and (b) The stacks were divided in two groups according to moment, and those within each group were averaged. The slower start and smoother shape for the smaller events are probably due to the greater effects of attenuation. (c) and (d) The stacks were divided into four groups and averaged. The lack of any clear trend with size other than that seen in (a) and (b) attests to the similarity of the events. The large and medium groups have $M_W \geq 6.3$.

such as this, in which time functions are normalized to a common seismic moment, attenuation has two salient effects.

First, it will have a greater effect on the scaled time functions of smaller events than on larger ones. Attenuation can be viewed as a filter operating over a fixed frequency band, whereas the corner frequency of the source spectrum increases as event moment decreases. Frequencies near the corner frequency carry the information about the gross time function shape. Thus, for smaller events, this information is attenuated more strongly than for larger events. The effect is to smooth out (that is, reduce the high-frequency detail of) time functions of the smaller events relative to the larger events. This effect can be seen in Figure 8, where the scaled time functions are displayed in order of increasing moment. However, even for some of the smallest events, a degree of complexity is noticeable, indicating that attenuation has not removed all the information about the shape of the time function in the size range of our events. Nonetheless, the shapes of the smallest events in this study should be viewed with the effects of attenuation in mind.

A second, smaller effect is the decrease in attenuation of teleseismic high-frequency energy as event depth increases. The effects of attenuation on the direct P wave decrease with increasing source depth because (1) the path length through the upper mantle decreases and (2) Q increases with depth. Thus, between 0.1 and 1 Hz, the attenuation suffered by a 600-km-deep event is about half that suffered by a shallow event [*Choy and Cormier*, 1986] because the teleseismic energy passes through the bulk of the upper mantle only once, on the way up. This is the main reason that body waves of deep earthquakes contain more high-frequency energy than those of shallow earthquakes. For body waves, the effects of attenuation (Q) are commonly modeled by the parameter t^*, which is often taken as a constant value. We estimate that an appropriate t^* for teleseismic P waves originating at a depth of 250 or 600 km is 0.5 or 0.35 s, respectively. The small difference between these values is indicative of the small difference in the effect of attenuation on deep and intermediate events.

To assess the first effect discussed above, that due to moment, we averaged the scaled time functions in different moment ranges to examine the effect of event size on the overall shape and on the rate of initiation of moment release. Figures 9 and 10 show averaged moment- and duration-scaled time functions, respectively. Duration

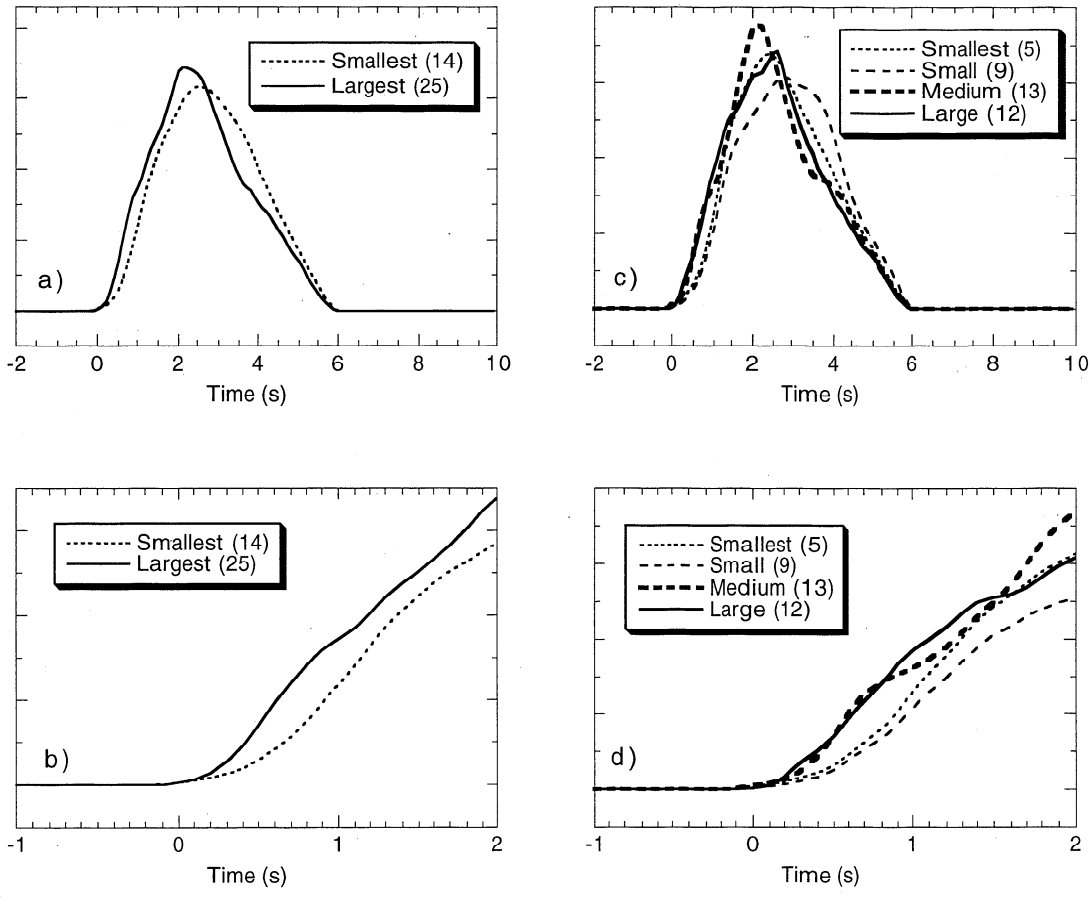

Figure 10. Averages of duration-scaled stacks grouped by event size. By definition, all duration-scaled time functions terminate at the reference time, 6 s (see text). In Figure 10c, attenuation appears to affect the shape of the small and smallest groups, but the average shape of the time functions of the medium and large groups is similar.

scaling is appropriate for averaging time functions to compare overall shape, whereas moment scaling may be more appropriate to compare other aspects, such as the rate of initiation and the relative durations and times of moment release. Averaging moment-scaled time functions inevitably produces a long tail due to the different scaled durations of the events (e.g., compare Figures 9 and 10). The slower start and smoother shape for the smaller events (Figures 9a and 10a) are probably due to the greater effects of attenuation on those events. No other clear trend is seen with increasing event size; in general, the events appear fairly self-similar over a wide range of sizes (Figure 10c).

With these stacks we observe a source from essentially one azimuth that depends, of course, on the location of the subduction zone. Thus the duration and subevent timing of a given stack depend somewhat on the angle between the azimuth from source to station and the direction of rupture propagation, which is, in general, unknown. The possible effect of directivity on our source time functions is difficult to quantify, but it seems unlikely that there are large systematic effects of directivity with depth in our data set. The takeoff angles of teleseismic *P* waves are fairly close to vertical; depending on the distance from the source to the stations, they range from 20° to 41° (from vertical) for events at 100 km depth and from 29° to 62° for events at 650 km depth. Thus any horizontal component of directivity present should not affect the waveforms strongly. We find no systematic differences between broadband stacks of events from different azimuths, although the number of events may be insufficient to discern small differences. Furthermore, directivity is, in general, relatively weak for intermediate and deep events. Compared to large shallow events on transform faults and subduction zones, deep and intermediate events are relatively compact, equant sources [e.g., *Fukao and Kikuchi*, 1987]. Figure 5 illustrates that for the largest events, those for which directivity is expected to be best resolved, the shapes, durations, and character of our broadband stacks correspond rather well to that of time functions determined from traditional inversion of data at many azimuths.

Finally, the different amounts of geometrical spreading experienced by P waves traveling different distances to receivers in North America will not affect our results because geometrical spreading is simply an amplitude effect, and we recover amplitude information by using the event moment, duration, and waveform, as discussed in section 3. Similarly, radiation pattern, which might vary somewhat across the arrays, generally affects the amplitude but not the shape of the waveforms (which is all we use from the broadband stack) and thus does not affect our time functions.

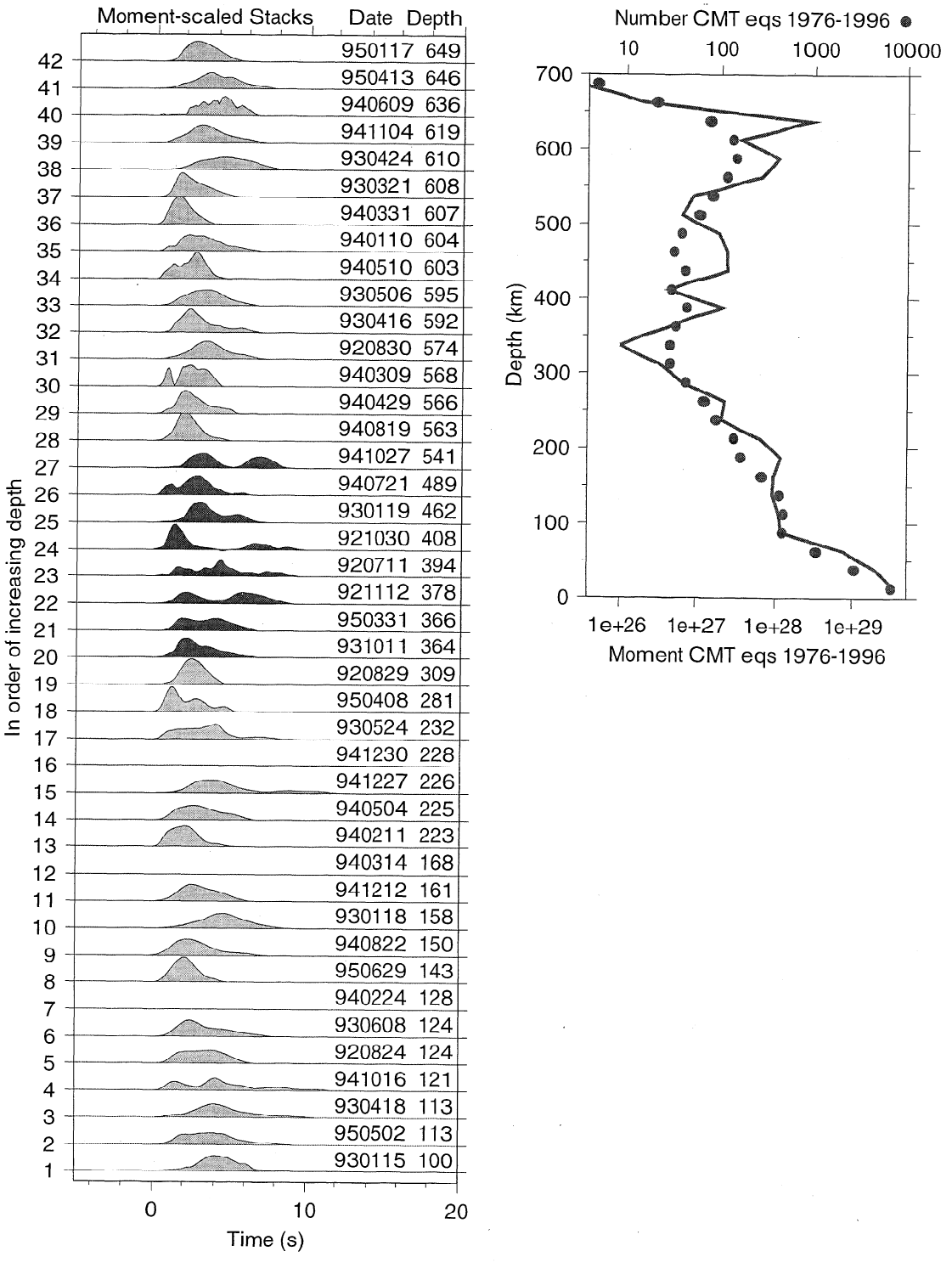

Figure 11. (left) Moment-scaled broadband stacks for all the events in this study. Events are shown in order of increasing depth from 100 to 650 km. Events with depths between 350 and 550 km (corresponding to depth indices from 20 to 27) have noticeably greater complexity in their time functions than shallower or deeper events. The area under each time function is the reference moment 10^{19} N m. Each increment on the y axis represents a moment-release rate of 5.7×10^{18} N m/s. Events 7, 12, and 16 are the events (3, 16, and 31 in moment index) which were omitted because they were judged too noisy or too nodal (see Figure 3). (right) Total moment (solid line) and number (dots) of Harvard CMT events from 1976 to 1996 versus depth.

5. Results: Variations of Time Functions With Depth and Moment

Perhaps the most salient feature of Figure 8 is the general similarity of the shapes of the time functions over a range of more than 3 orders of magnitude in moment; there is no large systematic change with moment beyond that expected from attenuation. Thus the scaling procedure works well, and the event durations are well-described by $M_0^{1/3}$ scaling (Figure 6a).

Figures 11 and 12 show moment- and duration-scaled time functions, respectively, obtained from broadband stacks in order of increasing depth. A weak decrease in moment-scaled duration (duration of the moment-scaled time function) with increasing depth is present in Figure 11, as in Figure 6b. In interpreting durations in Figure 11, it should be remembered that many of the events end gradually on the broadband records. The decrease of duration with depth seen here is similar to, though less strong than, that found by *Vidale and Houston* [1993] using only short-period stacks of about 130 events between 1980 and 1992. Vidale and Houston found a decrease in moment-scaled duration with depth from an average of 11 s at 100 km to 6 s at 600 km for the same reference moment used here, 10^{19} N m. However, that strong decrease was partly controlled by several intermediate-depth events of very long duration, a few of which appear to have been misinterpreted. The decrease of duration with depth found here (from 8.5 s at 100 km to 6.5 s at 600 km) is very similar to that found independently by *Bos et al.* [1998] by stacking broadband records globally for about 50 recent deep earthquakes. Studies of shallow earthquakes (using different data and techniques) found average scaled durations of 12 s [*Kanamori and Given*, 1981] and 10.2 s [*Ekstrom and Engdahl*, 1989; *Ekstrom*, 1987]; these are somewhat larger than what would be predicted by extrapolating the trend in Figure 6b.

The decrease in duration with depth is roughly inversely proportional to the increase in shear-wave velocity through the upper mantle (about 20%). This is consistent with the decrease expected assuming a constant stress drop model if the rupture propagation velocity is proportional to shear-wave velocity.

5.1 Greater Complexity and Late Moment Release in Events Between 350 and 550 km

An unexpected feature of Figures 11 and 12 is that the events between 350 and 550 km depth (those with depth index between 20 and 27) possess greater complexity in the shapes of their time functions, as well as more moment release toward the end of the rupture, than events shallower or deeper. Although some events above and below this depth range possess comparable complexity, each event between 350 and 550 km is complex. To our knowledge, this property has not been seen before and, indeed, would not be an easy feature to detect without a sufficient number of events and broadband waveform data, as well as our scaling procedures.

To examine this feature more closely, we divided the events into three groups based on their depth: "intermediate" from 100 to 350 km, "deeper" from 350 to 550 km, and "deepest" from 550 to 700 km. The average time function in each group was calculated for duration- and moment-scaled time functions (Figure 13). As mentioned in section 4, duration scaling is most appropriate for looking at the overall shape of scaled time functions because the average of moment-scaled time functions will intrinsically possess a tail due to the different moment-scaled durations of the individual time

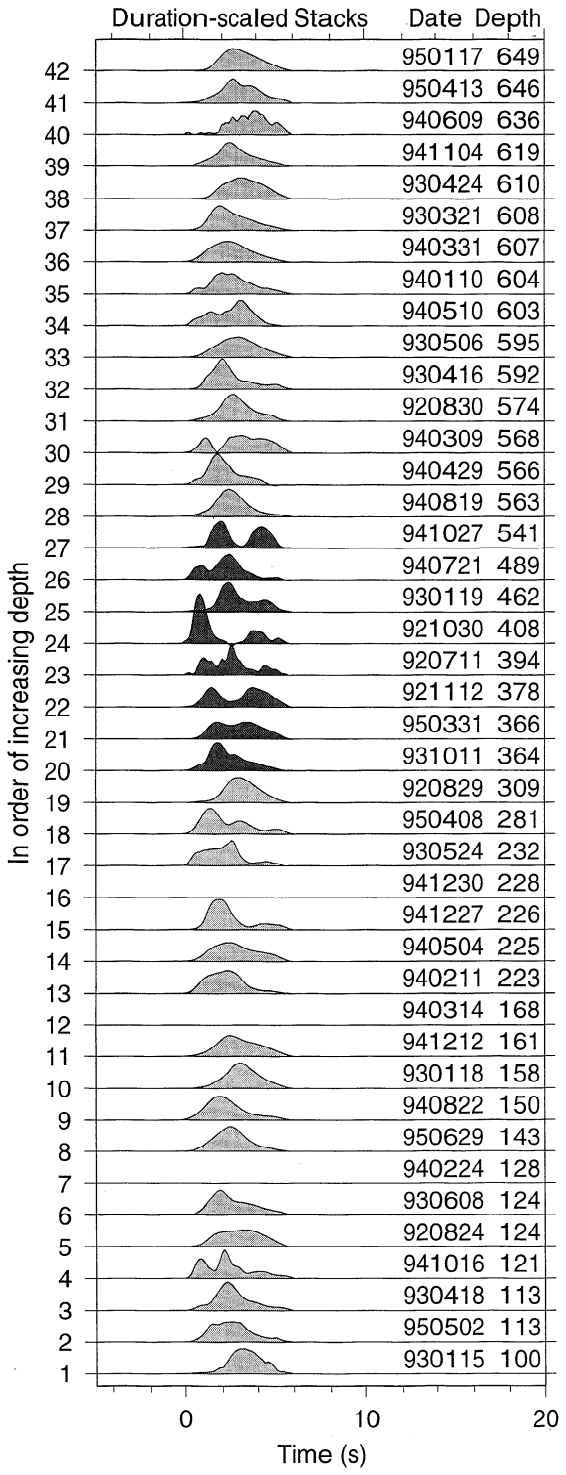

Figure 12. Similar to Figure 11, but with duration scaling. All scaled stacks have a duration of 6 s. The greater complexity of the events with depth indices 20 to 27 is evident, as in Figure 11.

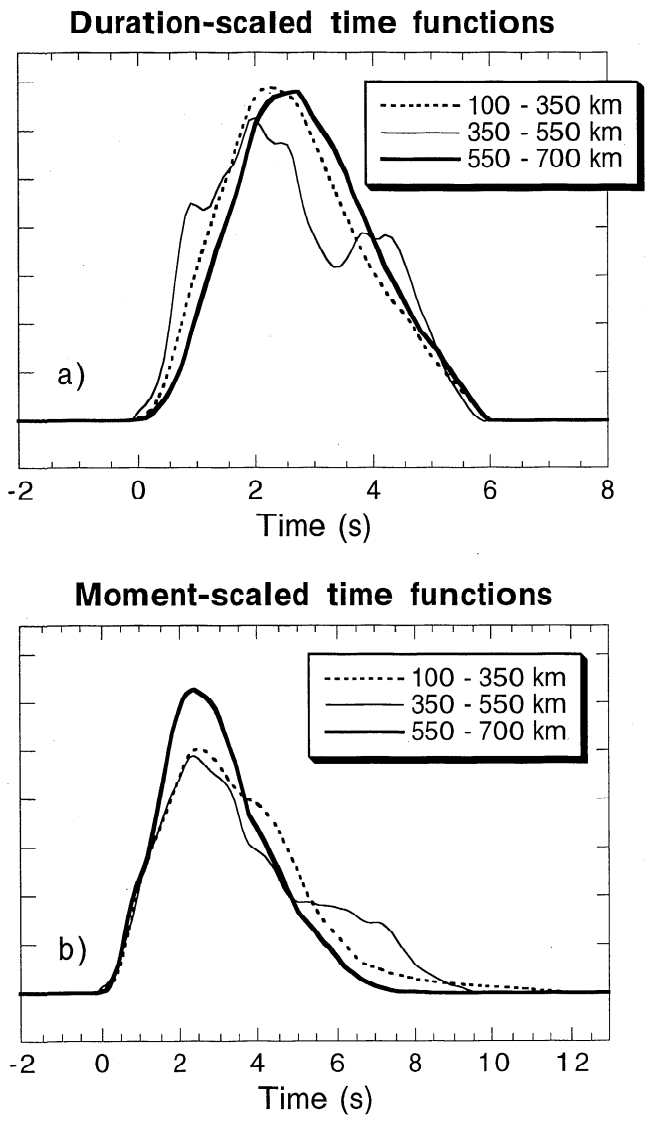

Figure 13. The average shapes of the time functions of intermediate, deeper and deepest groups of events. (a) Duration-scaled time functions. Duration scaling forces all stacks, and consequently, their averages to have a duration of 6 s. The greater complexity of the "deeper" events (those with depths between 350 and 550 km) is evident, as is the greater asymmetry of the intermediate events compared to the deepest ones (a perfectly symmetric time function would peak at 3 s). (b) Moment-scaled time functions. Events in the different depth groups initially grow at about the same rate, but the intermediate-depth events have the longest scaled duration and tail off more gradually than the deepest events.

functions averaged. Figure 13a shows the greater complexity of the deeper group, as well as somewhat greater asymmetry in time of the intermediate group compared to the deepest group. The later occurrence of the peak in the deepest group compared to the intermediate group is simply a consequence of the duration scaling and the longer tails of the intermediate group; in a perfectly symmetric one-peaked scaled time function the peak would occur at 3 s. This greater asymmetry is also seen in Figure 13b, which shows in addition the greater moment-scaled duration of the intermediate group. Greater asymmetry of intermediate events compared to the deepest ones was a central result of *Houston and Vidale* [1994]. Events in the different depth groups initially grow at about the same rate.

Complexity is a rather vague concept that is difficult to quantify. Another aspect of the "deeper" group of events is the occurrence of more moment release relatively late in the rupture (Figures 11 and 13b). A related aspect of the deeper time functions is the preponderance of two or more subevents of roughly similar moment, which are separated in time by a significant proportion of their duration. In fact, in itself this situation will result in slip later in the rupture if the subevents scale normally (i.e., if their duration is proportional to the cube root of their moment). To quantify this aspect, we filtered the moment-scaled time functions to remove the higher frequencies in scaled time (i.e., removed scaled frequencies $\geq$ 1 Hz), transformed displacements to velocities (i.e., took the time derivative) and counted zero crossings of the filtered time functions in velocity. Each zero crossing represents a change in the slope of the smoothed, scaled, displacement time function from positive to negative or vice versa and, as such, is a measure of complexity. The prevalence of multiple subevents in the "deeper" group compared to the others is manifest by more zero crossings of the velocity traces in this depth range (Figure 14a).

To further quantify aspects of the shape of the time functions, we computed their kurtosis and skewness [*Pollard*, 1977]. Kurtosis is a measure of the peakedness around its mean of a time series, and is defined as $\mu_4/(\mu_2)^2$, where μ_i is the ith moment about the mean (i.e., $\mu_i = \Sigma u(t)(t-\mu_1)^i$ for $i = 2, 3, 4, \ldots$ and μ_1 is the mean or centroid time). A large value of kurtosis indicates a time series strongly concentrated or peaked about its centroid time. Skewness, defined as $\mu_3/(\mu_2)^{3/2}$, measures the symmetry of a time series about its mean (i.e., centroid time). Because the centroid time is subtracted, skewness and kurtosis do not depend on how or even whether time functions are scaled. A skewness of 0 is associated with a perfectly symmetric time function. Skewness of earthquake time functions is usually positive, as most have tails. Most of our events have positive skewness (Figure 14b). The average skewness of the intermediate group is slightly larger than that of the deepest group, consistent with their greater asymmetry in time. In Figure 14b the deeper group of events is by no means entirely distinct from the other groups, but their kurtosis is, on average, smaller because they tend to be more spread out in time, consistent with their greater complexity; that is, most of the deeper group have multiple peaks and are thus less concentrated around a single peak.

It is unlikely that the greater complexity of the deeper group could be due to the effects of attenuation. If only the 25 largest events (those with moments $\geq 3.0 \times 10^{18}$ N m) are included, the result is very similar to Figure 13. It is also unlikely that the greater complexity of the "deeper" group could be the result of directivity. To produce the observed complexity in the deeper group by directivity would require that the relationship between the slip distribution and the azimuths from the events to the recording stations in North America happened to produce a complicated time function preferentially for events in that

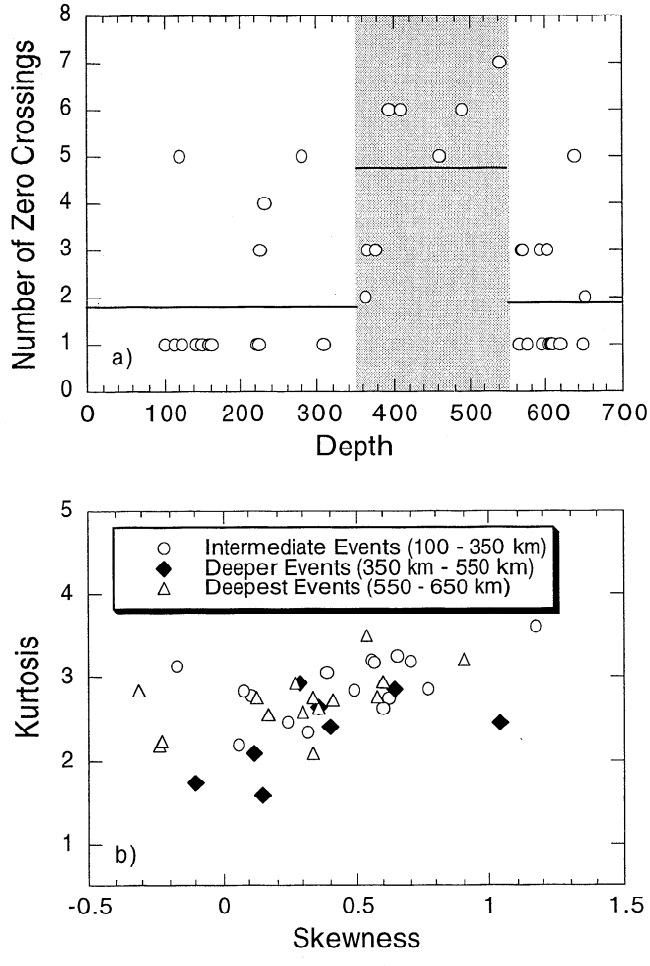

Figure 14. (a) The number of zero crossings of each time function (in velocity) versus depth. The number of zero crossings is a measure of complexity. The average number of zero crossings in each depth range is shown by a horizontal line. (b) Skewness versus kurtosis of the time functions grouped by depth. The greater complexity of shape for the deeper group of events (depths between 350 and 550 km) slightly reduces their kurtosis (peakedness) relative to the other events. The intermediate and deepest groups occupy very similar regions. Skewness is generally positive, as most earthquake time functions have tails.

group. However, the eight events in question occurred in three different subduction zones; on Figures 11 and 12, events 20 and 24 are from the Izu Bonin subduction zone, events 21, 25, and 26 are from Japan, and events 22, 23, and 27 are from Tonga. Furthermore, one intermediate (100-350 km) event from Izu Bonin (event 18) and several deep (550-700 km) events from Tonga (events 31, 36, 37, 38, and 42) appear quite simple. Moreover, to produce the observed complexity by directivity implicitly supposes that all time functions are complicated and that most are observed at an azimuth that fortuitously conceals their complex nature. Although difficult to assess quantitatively, it is unlikely that all deep events are complicated: previous studies of long-period and broadband *P* waves indicate that only about half of deep events are complex [e.g., *Fukao and Kikuchi*, 1987; *Sugi et al.*, 1989; *Houston and Williams*, 1991]. Similarly, in this study, about half of the events had only one zero crossing (Figure 14a) and can thus be characterized as simple.

5.2 Implications for Deep Failure Mechanisms

The greater complexity of events in the 350 to 550 km depth range, if real, is not yet understood. One possibility is that it may be related to greater structural complexity in the slab at those depths. Alternatively, it is suggestive of different physical mechanisms for events in the 350 to 550 depth range and the deepest events. *Kirby et al.* [1996] identified an "onset population" of events between 330 and 430 km depth based on a small peak in the number of large events in that depth range. This partially overlaps with our "deeper" group of events, and raises the possiblilty that both the onset events and the greater complexity of events between 350 and 550 km could be related to the onset of a regime of transformational faulting in metastable olivine.

Although speculative, a scenario in which seismic faulting between 350 and 550 km occurs by transformational faulting in metastable olivine [c.f. *Green and Houston*, 1995; *Kirby et al.*, 1996], while deeper seismicity occurs by a different mechanism, is compatible with recent thermal modeling of subducting slabs [*Kirby et al.*, 1996; *Devaux et al.*, 1997]. These thermal models have difficulty achieving cold enough temperatures to retain metastable olivine below about 550 km for most subducting slabs, the fast converging Tonga slab being the exception [see, e.g., *Kirby et al.*, 1996, Plate 3; *Devaux et al.*, 1997, Table 3]. Thus, in this scenario, metastable olivine is not presumed present below 550 km, except perhaps in Tonga. Consistent with this scenario is the possibility that the transformational faulting process itself may increase slab heterogeneity [*Frohlich*, 1987]. On the other hand, different mechanisms for the deeper and deepest groups of events (or indeed the deeper and intermediate groups) are not required by our observations. The scaled durations (Figure 6b) do not show a distinct change in trend at any depth.

5.3 Rate of Initiation of Moment Release

Recent work on the initiation of rupture of shallow events found a weak beginning to seismic moment release (termed "seismic nucleation phase") whose duration scales as the cube root of the total moment of the event, that is, as the total duration [*Ellsworth and Beroza*, 1995; *Beroza and Ellsworth*, 1996]. A nucleation phase that scales with event duration is unexpected in the context of current rate-and-state-dependent friction models [*Dieterich*, 1994]. Its presence was contested by *Mori and Kanamori* [1996], although clipping precluded a definitive test. Our data allow us to investigate whether a seismic nucleation phase is present systematically in deep and intermediate earthquakes.

Beroza and Ellsworth [1996] saw a systematic increase in the time between initiation of seismic slip and the start of high moment release rates (a "breakaway" phase) as magnitude increases [see *Beroza and Ellsworth*, 1996, Figure 3]; this is equivalent to a smaller average slope in the initial moment release rate of the larger events. We examined our time functions both before and after scaling to search for the systematic presence of a seismic nucleation phase. Figure 9 shows the effect of event size

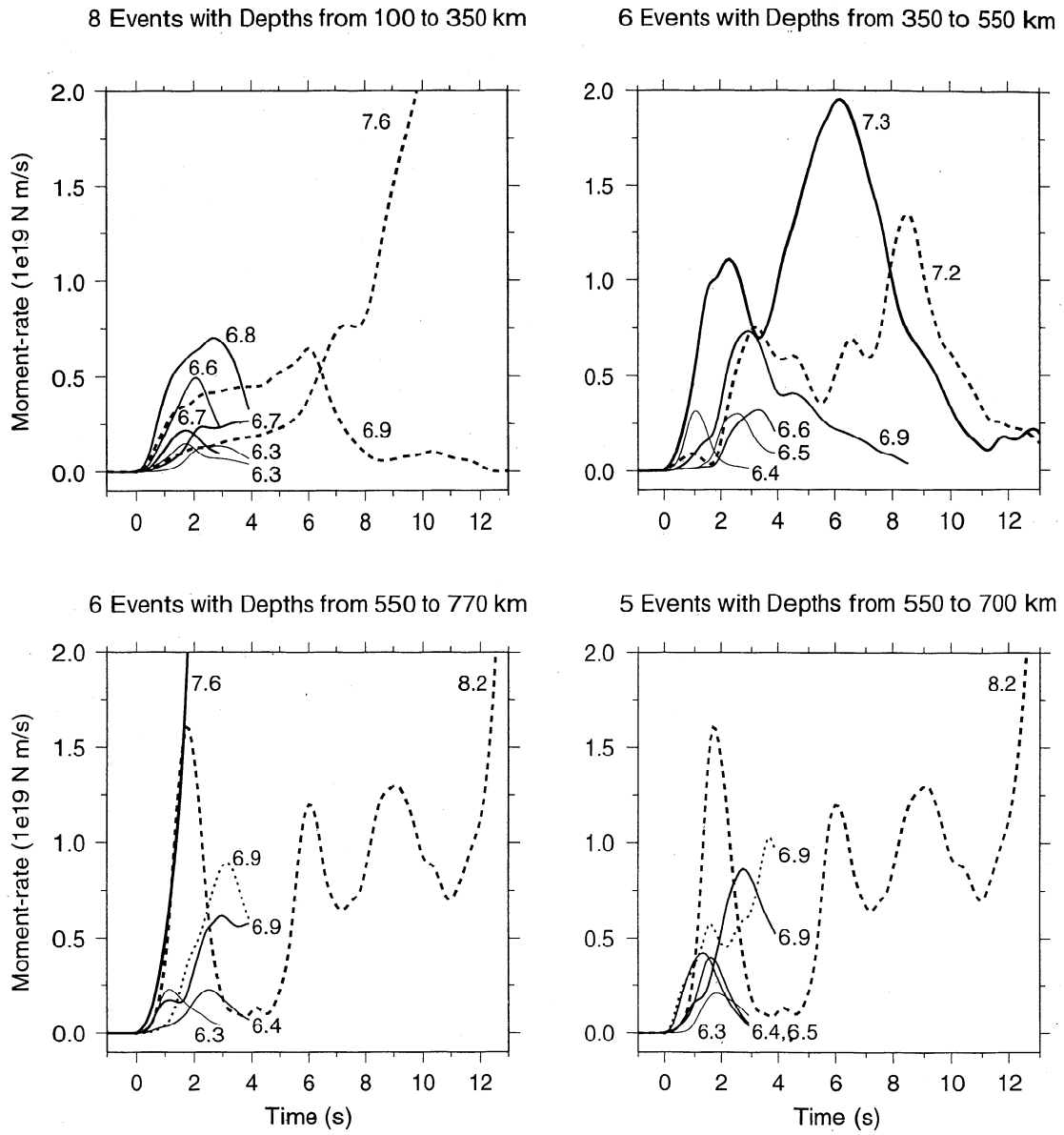

Figure 15. Comparison of earthquake initiations for all events with $M_W \geq 6.3$. The amplitudes of the displacement stacks have been scaled so that the areas under the waveforms are equal to the event moments; the time axes have not been scaled (that is, these are unscaled moment-rate functions). Events are divided into three depth ranges: 100-350 km, 350-550 km, and 550-700 km. Thicker lines are associated with larger events. The deep events are shown in two panels to reduce clutter, and the 1994 Bolivian time function is repeated in both bottom panels. A wide range of initiation behavior is seen, but, in general, large events start just as rapidly as smaller events.

on the average rate of initiation of moment release for moment-scaled time functions. *Ellsworth and Beroza's* [1995] seismic nucleation phase should occur over the first 1 to 2 s in the scaled time functions and entail smaller average slopes during the nucleation phase or a hiatus in moment release followed by a steeper breakaway phase. In Figure 9d the average stack of the "large" group has a brief hiatus in moment release rate around 1 s; however, the initial slope of the scaled stacks is increasing with event size. In this discussion, the behavior of the 14 smallest events is less relevant because, as noted above, their slower initiations may be mainly attributed to the effects of attenuation.

We also plot individual broadband stacks for the 25 events with $M_W \geq 6.3$ (Figure 15). These are not scaled time functions, but "true" moment-rate functions for which the area under the curve is equal to the event moment, as in the center of Figure 7. Seismic nucleation phases should be manifest by a decrease in the average slope of the initial moment-rate functions (displacement stacks) as event magnitude increases. Events of all sizes appear to start within the same wide range of slopes (Figure 15), with little indication of a systematic seismic nucleation phase with duration proportional to the cube root of event moment. In fact, there appears to be some increase in initial slope with increasing event magnitude consistent

with Figure 9d, although its significance is difficult to assess due to the large variability between events of similar magnitude.

The 1994 Bolivia earthquake merits special discussion. At M_W = 8.2, it is by far the largest event in this study (Figure 6). In the context of this paper, the scaled time function (event 40 on Figures 11 and 12) is not considered particularly complicated. The high-frequency complexity apparent in the scaled time function is simply the result of the event's large moment and low corner frequency; the apparent high frequencies in the scaled time function were originally much lower frequency waves that were not attenuated strongly. To check this aspect of the relation between event size and attenuation, we filtered the scaled time functions to a common passband in scaled time; plots analogous to Figures 11 and 12 had a smoother scaled time function for the Bolivian event but still showed relatively greater complexity for events between 350 and 550 km.

The 11 s long weak beginning of the Bolivian quake is unusual and, incidentally, causes the event's skewness to be negative. The weak beginning resembles the seismic nucleation phase of *Ellsworth and Beroza* [1995] in some ways. However, during the first 2 s of unscaled time, the Bolivian time function rises more rapidly than almost all of the other time functions (Figure 15). This behavior, reflected in Figure 9d, complicates the interpretation of such seismic nucleation phases.

5.4 Shapes of Short-Period Envelopes Compared With Broadband Stacks

Vidale and Houston [1993] and *Houston and Vidale* [1994] used only short-period stacks and their envelopes to study deep earthquake durations and time function shapes. The instrument response was not removed from the short-period data. Since the present study includes both types of data, it is interesting to compare the shapes of the envelopes of short-period stacks with those of the broadband stacks. For individual earthquakes the shapes are fairly similar in most cases (Figure 4). The average shapes are very similar, both for all events averaged together and in the three depth ranges (Figure 16), which validates the methodology of the previous studies, in particular, the use of short-period envelopes as proxies for average time functions. The greater complexity of the "deeper" events (those with depths between 350 and 550 km) is again evident.

6. Conclusions

Broadband and short-period stacks possess some of the same information about the source. The average shape of the envelopes of short-period stacks (without the instrument removed) is similar to that of broadband stacks of displacements. This can be useful in the many

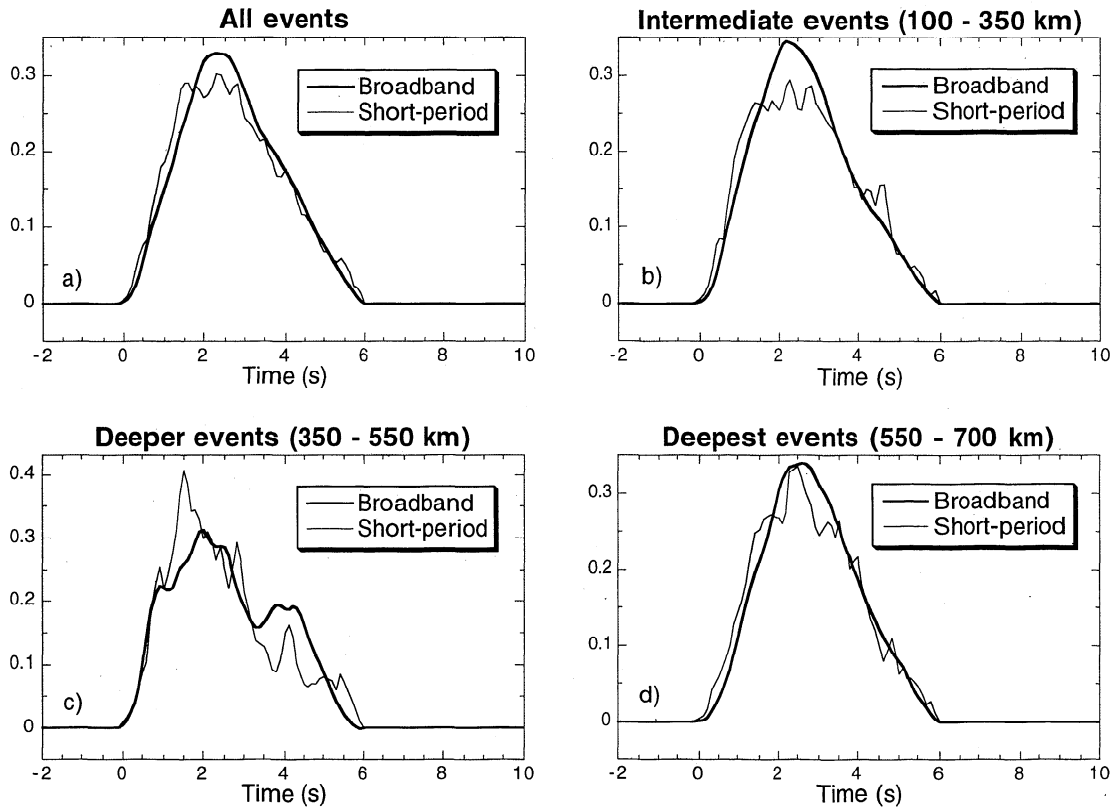

Figure 16. Comparison of the average shape of the broadband stacks with that of the scaled envelopes of short-period stacks. All stacks are duration-scaled to allow direct comparison of the overall shape. The average shapes are remarkably similar, considering that the instrument response has not been removed from the short-period stacks used to calculate the envelopes. The greater complexity of the "deeper" events (those between 350 and 550 km) is evident. (a) All events. (b) Sixteen intermediate-depth events. (c) Eight deeper events. (d) Fifteen deepest events.

situations in which broadband stations are sparse and short-period stations abundant. Despite the limitations of short-period data, short-period teleseismic waveforms from regional arrays can provide some unique information about the source because the greater number of stations leads to greater noise reduction upon stacking.

It is practical and useful to scale time functions to a common size for the purposes of comparison. Despite the simplicity of this procedure and the advantage it confers, it has not been done before, partly because it requires accurate estimation of event duration, and identification of the event termination from long-period or even broadband records is difficult. It is advantageous to use both broadband and short-period data, particularly in defining event termination and determining duration.

The main variations with depth in the time functions of the events studied here are (1) duration decreases more moderately with increasing depth than in the work by *Vidale and Houston* [1993] and is consistent with the increase of shear velocity with depth, (2) time functions of intermediate events have longer tails and are more asymmetric in time than those of deep events, as found by *Houston and Vidale* [1994], and (3) events between 350 and 550 km rupture with greater complexity, displaying more complicated time functions than most events above or below. These complicated time functions feature a significant amount of moment release later in the rupture (Figure 13b), suggestive of greater heterogeneity. In this regard, we note that 350 km depth corresponds to the onset of a possible regime of metastability in olivine and 550 km to the depth below which, according to recent thermal models, it would be difficult to retain metastable olivine for all except the Tonga slab.

Acknowledgments. We thank J. Evans and B. Julian for the *epick* software, which enabled interactive picking of features on which to line up the *P* waves. C. Mendoza, W. Spence, Associate Editor G. Beroza, and an anonymous referee made helpful comments on the manuscript. D. Sornette suggested counting zero crossings to quantify the time function shape. This work was supported by NSF grants EAR-9304553 and EAR-9601979 to H.H. and EAR-9628501 to J.E.V.

References

Abercrombie, R.E., Earthquake source scaling relationships from -1 to 5 M_L using seismograms recorded at 2.5 km depth, *J. Geophys. Res.*, *100*, 24,015-24,036, 1995.

Beroza, G.C., and W.L. Ellsworth, Properties of the seismic nucleation phase, *Tectonophysics*, *261*, 209-227, 1996.

Bos, A.G., G. Nolet, A. Rubin, H. Houston, and J.E. Vidale, Duration of deep earthquakes determined by stacking of Global Seismograph Network seismograms, *J. Geophys. Res.*, *103*, 21,059-21,065, 1998.

Choy, G.L., and V.F. Cormier, Direct measurement of the mantle attenuation operator from broadband *P* and *S* waveforms, *J. Geophys. Res.*, *91*, 7326-7342, 1986.

Chung, W.-Y., and H. Kanamori, Variation of seismic source parameters and stress drops within a descending slab and its implications in plate mechanics, *Phys. Earth Planet. Inter.*, *23*, 134-159, 1980.

Devaux, J.P., G. Schubert, and C. Anderson, Formation of a metastable olivine wedge in a descending slab, *J. Geophys. Res.*, *102*, 24,627-24,637, 1997.

Dieterich, J., A constitutive law for rate of earthquake production and its application to earthquake clustering, *J. Geophys. Res.*, *99*, 2601-2618, 1994.

Dziewonski, A.M., and J.H. Woodhouse, An experiment in systematic study of global seismicity: Centroid-moment tensor solutions for 201 moderate and large earthquakes of 1981, *J. Geophys. Res.*, *88*, 3247-3271, 1983.

Ekstrom, G., and E.R. Engdahl, Earthquake source parameters and stress distribution in the Adak Island region of the central Aleutian Islands, Alaska, *J. Geophys. Res.*, *94*, 15499-15519, 1989.

Ekstrom, G., A broad band method of earthquake analysis, Ph. D. thesis, Harvard Univ., Cambridge, Mass., 1987.

Ellsworth, W.L., and G.C. Beroza, Seismic evidence for an earthquake nucleation phase, *Science*, *268*, 851-855, 1995.

Frohlich, C., Aftershocks and temporal clustering of deep earthquakes, *J. Geophys. Res.*, *92*, 13944-13957, 1987.

Frohlich, C., The nature of deep earthquakes, *Annu. Rev. Earth Planet. Sci.*, *17*, 227-254, 1989.

Fukao, Y., and M. Kikuchi, Source retrieval for mantle earthquakes by iterative deconvolution of long-period *P* waves, *Tectonophysics*, *144*, 249-269, 1987.

Furumoto, M., and I. Nakanishi, Source times and scaling relations of large earthquakes, *J. Geophys. Res.*, *88*, 2191-2198, 1983.

Green, H.W., and P.C. Burnley, A new self-organizing mechanism for deep-focus earthquakes, *Nature*, *341*, 733-737, 1989.

Green, H.W., and H. Houston, The mechanics of deep earthquakes, *Annu. Rev. Earth Planet. Sci.*, *23*, 169-213, 1995.

Green, H.W., T.E. Young, D. Walker, and C.H. Scholz, Anticrack-associated faulting at very high pressure in natural olivine, *Nature*, *348*, 720-722, 1990.

Griggs, D.T., and D.W. Baker, The origin of deep focus earthquakes, in *The Properties of Matter*, pp. 23-42, John Wiley, New York, 1969.

Hobbs, B.E., and A. Ord, Plastic instabilities: Implications for the origin and intermediate and deep focus earthquakes, *J. Geophys. Res.*, *93*, 10521-10540, 1988.

Houston, H., Deep earthquakes shake up debate, *Nature*, *372*, 724-725, 1994.

Houston, H., and J.E. Vidale, The temporal distribution of seismic radiation during deep earthquake rupture, *Science*, *265*, 771-774, 1994.

Houston, H., and Q. Williams, Fast rise times and the physical mechanism of deep earthquakes, *Nature*, *352*, 520-522, 1991.

Ihmle, P.F., and T.H. Jordan, Source time function of the great 1994 Bolivia deep earthquake by waveform and spectral inversions, *Geophys. Res. Lett.*, *22*, 2253-2256, 1995.

Kanamori, H., and D.L. Anderson, Theoretical basis for some empirical relations in seismology, *Bull. Seismol. Soc. Am.*, *65*, 1073-1095, 1975.

Kanamori, H., and J.W. Given, Use of long-period surface waves for rapid determination of earthquake source parameters, *Phys. Earth Planet. Inter.*, *27*, 8-31, 1981.

Kanasewich, E.R., *Time Series Analysis in Geophysics*, 480 pp., Univ. of Alberta Press, Edmonton, Alberta, 1981.

Kikuchi, M., and Y. Fukao, Inversion of long-period *P* waves from great earthquakes along subduction zones, *Tectonophysics*, *144*, 231-247, 1987.

Kirby, S.H., Localized polymorphic phase transformation in high-pressure faults and applications to the physical mechanism of deep-focus earthquakes, *J. Geophys. Res.*, *92*, 13789-13800, 1987.

Kirby, S.H., W.B. Durham, and L.A. Stern, Mantle phases changes and deep earthquake faulting in subducting lithosphere, *Science*, *252*, 216-225, 1991.

Kirby, S.H., S. Stein, E.A. Okal, and D.C. Rubie, Metastable mantle phase tranformations and deep earthquakes in subducting oceanic lithosphere, *Rev. Geophys.*, *34*, 261-306, 1996.

McGuire, J.J., D.A. Wiens, P.J. Shore, and M.G. Bevis, The March 9, 1994 (M_w 7.6) deep Tonga earthquake: Rupture

outside the seismically active slab, *J. Geophys. Res.*, *102*, 15,163-15,182, 1997.

Meade, C., and R. Jeanloz, Acoustic emissions and shear instabilities during phase transformation in Si and Ge at ultrahigh pressure, *Nature*, *339*, 616-618, 1989.

Mikumo, T., Source process of deep and intermediate earthquakes as inferred from long-period *P* and *S* waveforms, 2. Deep-focus and intermediate-depth earthquakes around Japan, *J. Phys. Earth*, *19*, 303-320, 1971.

Mori, J., and H. Kanamori, Initial rupture of earthquakes in the 1995 Ridgecrest, California sequence, *Geophys. Res. Lett.*, *23*, 2437-2440, 1996.

Ogawa, M., Shear instability in a viscoelastic material as the cause of deep focus earthquakes, *J. Geophys. Res.*, *92*, 13801-13810, 1987.

Pollard, J.H., *A Handbook of Numerical and Statistical Techniques*, Cambridge Univ. Press, New York, 1977.

Scholz, C.H., *The Mechanics of Earthquakes and Faulting*, 439 pp., Cambridge Univ. Press, New York, 1990.

Silver, P.G., S.L. Beck, T.C. Wallace, and C. Meade, Rupture characteristics of the deep Bolivian earthquake of 9 June 1994 and the mechanism of deep-focus earthquakes, *Science*, *268*, 69-73, 1995.

Stein, S., Deep earthquakes: A fault too big?, *Science*, *268*, 49-50, 1995.

Sugi, N., M. Kikuchi, and Y. Fukao, Mode of stress release within a subducting slab of lithosphere: Implication of source mechanism of deep and intermediate-depth earthquakes, *Phys. Earth Planet. Inter.*, *55*, 106-125, 1989.

Sung, C.M., and R.G. Burns, Kinetics of the olivine-spinel: Implications to deep-focus earthquake genesis, *Earth Planet. Sci. Lett.*, *32*, 165-170, 1976.

Vidale, J.E., and H. Houston, The depth dependence of earthquake duration and implications for rupture mechanisms, *Nature*, *365*, 45-47, 1993.

Wadati, K., Shallow and deep earthquakes, *Geophys. Mag.*, *1*, 162-202, 1928.

Wiens, D.A., J.J. McGuire, P.J. Shore, M.G. Bevis, K. Draunidalo, G. Prasad, and S. Helu, A deep earthquake aftershock sequence and implications for the rupture mechanism of deep earthquakes, *Nature*, *372*, 540-543, 1994.

H. M. Benz, U.S. Geological Survey, POB 25046, MS 966, Denver, CO 80225. (benz@gldfs.cr.usgs.gov)

H. Houston and J. E. Vidale, Department of Earth and Space Sciences, 595 Circle Drive East, University of California, Los Angeles, CA 90095-1567. (hhouston@ess.ucla.edu; vidale@ucla.edu)

(Received July 28, 1997; revised May 11, 1998;
accepted June 18, 1998.)